SANDIA REPORT

SAND2006-5098
Unlimited Release
Printed August, 2006

Surface-wave and refraction tomography at the FACT Site, Sandia National Laboratories, Albuquerque, New Mexico

Robert E. Abbott, Lewis C. Bartel, Bruce P. Engler, Satish Pullammanappallil

Prepared by
Sandia National Laboratories
Albuquerque, New Mexico 87185 and Livermore, California 94550

Sandia is a multiprogram laboratory operated by Sandia Corporation,
a Lockheed Martin Company, for the United States Department of Energy's
National Nuclear Security Administration under Contract DE-AC04-94-AL85000.

Issued by Sandia National Laboratories, operated for the United States Department of Energy by Sandia Corporation.

Available to DOE and DOE contractors from
U.S. Department of Energy
Office of Scientific and Technical Information
P.O. Box 62
Oak Ridge, TN 37831

Telephone: (865) 576-8401
Facsimile: (865) 576-5728
E-Mail: reports@adonis.osti.gov
Online ordering: http://www.osti.gov/bridge

Available to the public from
U.S. Department of Commerce
National Technical Information Service
5285 Port Royal Rd.
Springfield, VA 22161

Telephone: (800) 553-6847
Facsimile: (703) 605-6900
E-Mail: orders@ntis.fedworld.gov
Online order: http://www.ntis.gov/help/ordermethods.asp?loc=7-4-0#online

SAND2006-5098
Unlimited Release
Printed August, 2006

Surface-wave and refraction tomography at the FACT Site, Sandia National Laboratories, Albuquerque, New Mexico

Robert E. Abbott
Solid Dynamics and Energetic Materials Department
Sandia National Laboratories
P.O. Box 5800
Albuquerque, NM 87185-1168

Lewis C. Bartel, Bruce P. Engler
Geophysics Department
Sandia National Laboratories
P.O. Box 5800
Albuquerque, NM 87185-0750

Satish Pullammanappallil
Optim, Inc., MS 174
1664 N. Virginia St., Reno, NV 89557-0141

Abstract

We present a technique that allows for the simultaneous acquisition and interpretation of both shear-wave and compressive-wave 3-D velocities. The technique requires no special seismic sources or array geometries, and is suited to studies with small source-receiver offsets. The method also effectively deals with unwanted seismic arrivals by using the statistical properties of the data itself to discriminate against spurious picks. We demonstrate the technique with a field experiment at the Facility for Analysis, Calibration, and Testing at Sandia National Laboratories, Albuquerque, New Mexico. The resulting 3-D shear-velocity and compressive-velocity distributions are consistent with surface geologic mapping. The averaged velocities and V_p/V_s ratio in the upper 30 meters are also consistent with examples found in the scientific literature.

Acknowledgments

The authors thank Bob Reinke, Al Leverette, and Robert Rodriguez of the Defense Threat Reduction Agency for the loan of their accelerated weight-drop seismic source and for their assistance with the field work. We also thank the IRIS Passcal Instrument center for the loan of two seismographs and the seismic sensors. Robert Greschke of the Instrument Center helped with the field work and took the pictures for Figures 3 and 4. Richard Kromer, of Sandia Labs, facilitated access to the FACT site and helped with logistics. Partial funding for this report was furnished under the Near Real Time Characterization for Assured HDBT Defeat Grand Challenge LDRD at Sandia National Laboratories.

Contents

List of Figures

Introduction

Detailed knowledge of shallow shear-wave velocity structure is particularly useful in a number of contexts. For example, shear-wave velocity in the upper 30 meters is a key parameter for seismic hazard ground-motion predictions (Frankel et al., 1996). When compared to compressional-wave velocities, the ratio V_p/V_s is sensitive to porosity, fracturing, fluid content, and composition of the host rock(e.g., Tatham (1982); Domenico (1984); Ensley (1985); Arns et al. (2002)). Although useful, shear-wave experiments are relatively uncommon because they can be difficult to interpret and often require (or at least greatly benefit from) the use of a shear-wave generating source. These sources have the benefit of preferentially exciting shear waves relative to compressional waves, and are desired when the analyst is faced with picking S-wave arrivals in the individual seismograms. However, if P-wave data is also required, a second source is necessary, increasing the fielding time and data volume to be analyzed. A technique that uses the same geometry, source, and data as a standard P-wave tomographic survey, yet yields S-wave velocities as well, would be an improvement. For this reason, recent years have seen an increase in techniques designed to exploit the properties of surface-waves (Louie, 2001; Park et al., 1999; Nazarian and Stokoe II, 1984), as surface waves are sensitive to the shear-wave velocity of the medium in which they propagate.

Surface waves have several properties that make them useful for shallow site characterization. Firstly, they are easy to generate as most of the energy from an impulsive, surface source goes to the creation of surface waves. Secondly, their dispersive property allows for quantification of velocity with depth, including "thin" layers and velocity inversions. Thirdly, as previously mentioned, surface waves are mostly sensitive to shear velocity, a key parameter in engineering and seismic hazard studies. Lastly, the same geometries and acquisition parameters used for the collection of refraction and reflection data is often suited to surface-wave studies. This allows for the possibility of characterization of both compressive and shear velocities using the same set of data.

This report summarizes a field experiment at the Facility for Analysis, Calibration, and Testing (FACT) Site at Sandia National Laboratories in Albuquerque, New Mexico. A goal of the study was to examine ways to acquire and analyze simultaneous compressional- and surface-wave data for 3-D characterization of the shallow subsurface.

Experiment

Geologic Setting

The Facility for Analysis, Calibration, and Testing (FACT) Site at Sandia National Laboratories is located on eastern edge of the Albuquerque basin, just south of the city of Albuquerque, New Mexico, USA (Figure 1). The Albuquerque basin is a sedimentary basin within the Rio Grande rift, a large continental rift extending from Chihuahua, Mexico, to central Colorado. The rift primarily formed in two pulses of extension, first 30-20 m.y. before present, and then 9-6 m.y. before present (Olsen et al., 1987). The recording site occupies a reentrant into the Manzanita Mountains, with bedrock outcropping less than 1 km to the east and south. Bedrock at this latitude of the Manzanitas consists primarily of the Proterozoic Manzanita Granite, overlain unconformably by the shales and siltstones of the Pennsylvanian-Permian Madera Formation (Dane and Bachman, 1965; Chamberlin et al., 2002). The FACT Site sits on a topographical bench, the Hubbell bench (Pazzaglia et al. (1999, Fig. 2)), formed by en echelon, down-to-the-east normal faults. The bounding fault on the east is the older, range-forming Manzano fault ($\approx$ 1.5 km distant); on the west is the younger intra-basin Hubbell Springs fault ($\approx$ 5 km distant) (Personius et al., 1999; Maldonado et al., 1999). Geology at the surface consist of partially cemented piedmont deposits of early- to middle-Pleistocene age, obscuring the bedrock (Chamberlin et al., 2002). The deposits form a broad, flat-topped hill 5-10 meters above neighboring, younger alluvial deposits. Topography on our 100 meter by 70 meter grid is generally planar with a slight downward tilt to the northwest. Depth-to-bedrock is not precisely known, but unlogged boreholes at the site penetrated "fractured granite" (i.e., Manzanita Formation) at approximately 40-meters depth (R. Kromer, personal communication, 2005).

Data Acquisition

Sensor geometry at the FACT Site consisted of 3 laydowns of up to 119 4.5 Hz, single-component vertical geophones (Figure 2), hooked to 2 Geometrics StrataView 60-channel seismographs (instruments courtesy of the IRIS Passcal Instrument Center, Soccoro, New Mexico). Station spacing was a regular 5-meter grid, designed to fully occupy the fenced portion of the FACT Site, approximately 100 meters by 70 meters (Figure 3). Because buildings and other infrastructure occasionally occupied grid nodes, the grid had a few gaps. In total, 323 sensors were deployed among the three laydowns. The seismic source was a GiscoGeo ESS100 accelerated weight-drop and metal plate (Figure 4). Ten shots were vertically stacked at 16 locations within, and just without, the sensor grid. In order to record data at all sensors, each source point had to be re-occupied three times, once for each laydown. Data was recorded at a sample rate of 1000 Hz for 5 seconds, with only an anti-alias filter in place.

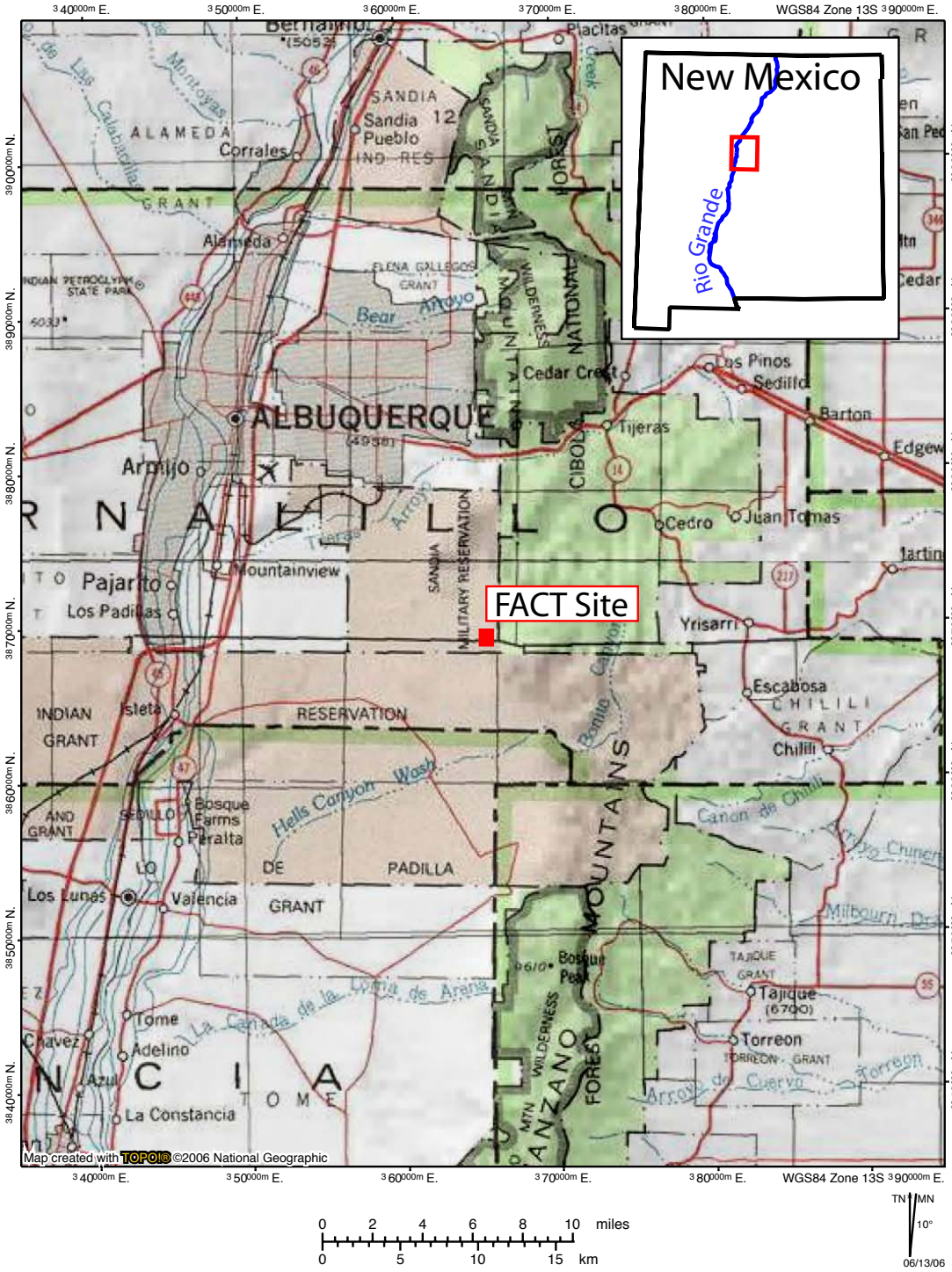

Figure 1. Location map for the Facility for Analysis, Testing, and Calibration (FACT) Site at Sandia National Laboratories

Figure 2. The 4.5-Hz geophones were wired in serial in groups of six (a technique to reduce surface waves when fully strung out). This required us to plant all six in the same location to simulate one sensor. Sensors and seismographs were loaned by the IRIS Passcal Instrument Center.

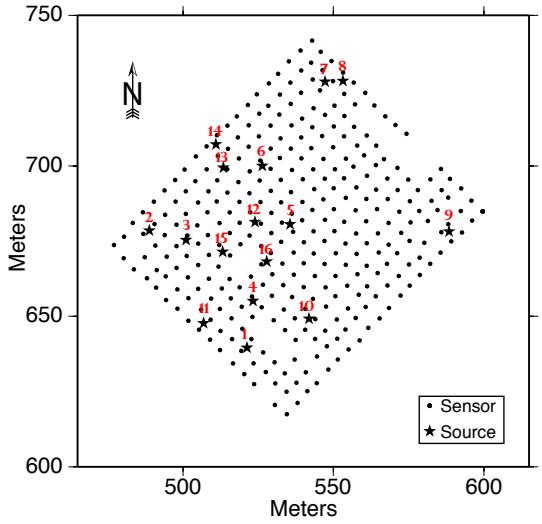

Figure 3. Experiment Layout at the FACT Site. Black circles are 4.5-Hz geophones, numbered stars are accelerated weight-drop source locations.

Figure 4. Accelerated weight-drop and metal plate, loaned by the Defense Threat Reduction Agency.

Method

Method Outline

A brief outline of our processing flow is as follows. Each step will be discussed further in sections below.

1. Surface-wave Tomography

   (a) The first step is to pick the local maxima of the analytic-signal amplitude for each source-receiver pair at regular frequency intervals for the frequency range of interest. The number of picks made is limited either by the total number of local maxima in the trace, or all the maxima up to a user-defined value.

   (b) As the picks in the previous step may represent arrivals other than the fundamental Rayleigh wave (or noise spikes) the second step is to define the proper velocity range for fundamental surface-wave propagation. This is accomplished by imaging the average 1-D surface-wave dispersion curve for the area of interest, and creating a velocity window bounding the fundamental-mode propagation. Picks from Step 1 falling outside this window are discarded.

(c) The time picks for all receivers in the fundamental Rayleigh-wave time window at a given frequency are then used to create a 2-D tomogram of group velocity for that frequency. Combining the tomograms for all frequencies creates a 3-D volume of group velocity at x, y, f. Now, each x, y grid coordinate is associated with a frequency-dependent group velocity (i.e., a conventional group-velocity dispersion curve).

(d) The individual dispersion curves from Step 3 are then inverted for S-wave velocity versus depth. These individual inversions are then gridded to form a 3-D volume of shear-wave velocity at x, y, z, where z represents depth below the surface.

2. Refraction Velocity Optimization

   (a) For each source-receiver pair, pick the first arrival and compute traveltimes.

   (b) Invert first-arrival traveltimes for 3-D P-wave velocity using a simulated-annealing, non-linear optimization algorithm (SeisOpt® by Optim, LLC).

Surface-Wave Tomography

Surface waves travel at velocities that are controlled by their wavelengths. Longer wavelength, and hence lower frequency, waves penetrate deeper than shorter wavelength, higher frequency, waves. In areas of varying velocity with depth, the relationship of frequency versus velocity for a surface-wave train is called a dispersion curve. Since our goal is to create a 3-D model of velocity, dispersion curves from each source-receiver raypath is needed. As noted in Kocaoglu and Long (1993), there are several widely-used techniques to pick the frequency-dependent surface-wave velocities. Some of the techniques that work well in global or regional studies of surface-wave propagation, are unsuited to the scale of this experiment (maximum offset of approximately 100 meters). This is because the surface waves do not separate sufficiently in time from the faster body waves, be they direct, reflected off shallow layers, or refracted. We found the multiple filter technique (MFT) of Dziewonski et al. (1969), to yield good results.

The MFT consists of computing the amplitude of the analytic signal at a number of discrete frequencies. In our processing flow, the de-trended, Hamming-windowed, and Fourier-transformed input seismograms are filtered by a series of narrow bandpass filters. The filter of choice is a Gaussian filter, $G_n(\omega)$, of the form

$$G_n(\omega) = F(\omega) \exp\left[-\alpha \left(\frac{\omega - \omega_n}{\omega_n}\right)^2\right]. \tag{1}$$

where $F(\omega)$ is the FFT of the input seismogram, ω_n is the center frequency of the filter, and α is the bandwidth parameter. As in Dziewonski et al. (1969), a Gaussian filter is

chosen because it has the greatest time-frequency resolution of any non-band-limited function. The seismograms are filtered in both the forward and reverse directions for zero phase distortion. Filtered output of each trace is created at 1-Hz intervals, from the minimum to the maximum frequency of interest. Still in the frequency domain, we calculate the quadrature spectrum $Q_n(\omega)$,

$$Q_n(\omega) = G_n(\omega)e^{i\omega\frac{\pi}{2}}. \tag{2}$$

After inverse FFT such that $Q_n(\omega) \rightarrow q_n(t)$ and $G_n(\omega) \rightarrow g_n(t)$, the instantaneous amplitude A_n at time t is given by

$$A_n(t) = [g_n^2(t) + q_n^2(t)]^{\frac{1}{2}}. \tag{3}$$

All local maxima $A_n(t)$ are picked as possible fundamental-mode Rayleigh-wave arrivals. In most cases, the local maxima with the highest amplitude is the correct choice. However, there are some situations where this is not the case. Surface-wave higher modes, direct arrivals, and other seismic phases can be locally stronger. In addition, noise spikes can be a source of contamination. Higher-mode surface waves are a particular problem when there are subsurface velocity reversals or layers with especially high velocity contrasts (O'Neill and Matsuoka, 2005). Most of these arrivals have unreasonable fundamental-mode Rayleigh-wave velocities and can be discarded. To define the reasonable velocity, we compute a 1-D average dispersion curve of the entire region for which we have ray coverage.

This 1-D average dispersion is calculated by simply collecting all the calculations of group velocity versus frequency for the entire region of interest and and examining their distribution. Instances of raypaths through anomalously low or high velocities will distribute at the fringes of the averaged value. An envelope can be defined that captures the expected range of velocities, but still discriminates against spurious picks caused by noise or other seismic phases. One way to define the bounds of the envelope is to find the velocity window that contains a given percentage of all picks for that frequency. A window that contains 95% of the picks (a 2σ criteria, if the distribution is approximately normal) works well in most cases.

Next, we gather all picks for a given frequency that fall within within the defined time window. The tomographic inversion code PRONTO (Aldridge and Oldenburg, 1993) was used two reconstruct a 2-D velocity field from the group-wave traveltimes. The inversion for each frequency is done separately. PRONTO uses the finite-difference method of Vidale (1988) to calculate traveltimes to every point on a slowness grid, using planar-wavefront traveltime operators. Curved raypaths through the traveltime field are calculated by the method of steepest descent. Before inversion, constraints are defined in order to decrease non-uniqueness. These constraints can be physical (e.g., borehole velocities or other groundtruth), or qualitative (e.g., preference for smoothly varying velocities). We lacked adequate ground truth, so the model was

not physically constrained. However, we applied regularization constraints on the first and second derivatives of the model following the scheme laid out in Aldridge and Oldenburg (1993).

The 2-D tomograms for each frequency can then be combined to create a 3-D volume in x, y, and f, where x and y are easting and northing, respectively. Viewed this way, every coordinate has a velocity associated with every frequency, defining a dispersion curve at each x, y location. These individual dispersion curves, one for each grid node, are then separately inverted for shear-wave velocity with depth in the following step.

The inversion of the dispersion curves for shear-wave velocity follows an iterative process. First, a starting model is chosen and used to calculate a dispersion curve. The starting model can be an educated guess, but in our case was the result of inverting the average 1-D dispersion of the region. The forward model is created with the program SURF96 (Herrmann, 2005). The key parameters for the laterally homogeneous starting model are layer thickness h, layer shear-wave velocity v_s, layer pressure-wave velocity, v_p, and layer density ρ , with h and v_s being the most sensitive. Next, perturbations to the initial model are calculated for each x, y location. The four key parameters are randomly perturbed (within wide, but reasonable, limits) and the RMS fit to the data at the x, y location is calculated.

Once 10 randomly perturbed models that were within a user-defined RMS error range are found, the best model is forwarded to a standard Marquardt inversion. During this, or any other, stage of the inversion process, if the updated model falls within a global RMS limit the inversion process is stopped and the model accepted. If, after 30 iterations of the Marquardt inversion the global RMS error limit is not reached, the best model is forwarded to a constrained-random inversion.

In the constrained-random phase of the inversion, the best model from the Marquardt inversion serves as a new starting model about which new random models are created. The purpose of this phase is to jump the model out of any local minimum it might be in. As before, models with reduced RMS error are accepted and the inversion is stopped if the global RMS limit is reached. The best of 10 models is then reintroduced to the Marquardt inversion with a reduced damping factor.

If three iterations of the combined Marquardt/constrained-random inversion process fails to satisfy the RMS limit, a final series of random perturbations of decreasing magnitude is attempted. If the RMS error is not improved after 60 iterations, or the magnitude of the perturbation falls below a user-defined value, the inversion for that x, y location is flagged as incomplete.

Finally, the individual 1-D models for locations x, y are stitched together to make a 3-D volume of shear-wave velocity versus depth. Because the layer thicknesses of the individual 1-D models vary from location to location, a uniform layer thickness is chosen and the models are gridded using a nearest-neighbor algorithm. Gaps in the data volume caused by 1-D inversion failures are also smoothed over in this way.

Refraction Velocity Optimization

The refraction-tomography processing flow is conceptually more simple. In an area of increasing seismic velocity with depth, the first arrival on a seismogram is either a direct or refracted (bent towards the surface by increasing velocity) P-wave. In this study, reconstruction of the 3-D P-wave velocity structure is achieved using a simulated-annealing non-linear optimization algorithm (specifically the program SeisOpt®, a commercial product by Optim, LLC). The simulated-annealing algorithm is a Monte Carlo-based process that is adapted to finding the global minimum of a non-linear problem. It has the benefit of being insensitive to the starting model, so a good initial "guess" is not needed. Input parameters are simply the source-receiver geometries and first-arrival traveltimes. As with the surface-wave tomography, travel times are calculated using the Vidale (1988) finite-difference scheme. In practice, some fine tuning of the inversion parameters (such as the "temperature", iteration limits, etc.) are needed for satisfactory results. A general discussion of these and other details is discussed in Pullammanappallil and Louie (1994).

Results

Raw Data

Figures 5 and 6 show a raw shot-gather and an individual raw trace, respectively. As can be seen, the signal-to-noise ratio was excellent, and the raw trace shows a clear first-arrival and nicely-developed surface wave. The move-out pattern on the shot-gather is the result of the lines looping back and forth (NE-SW) within the fenced-in FACT Site.

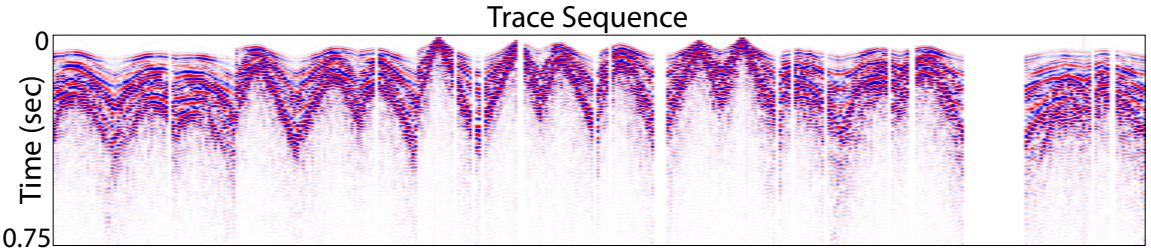

Figure 5. A raw shot-shotgather of one source to all sensors.

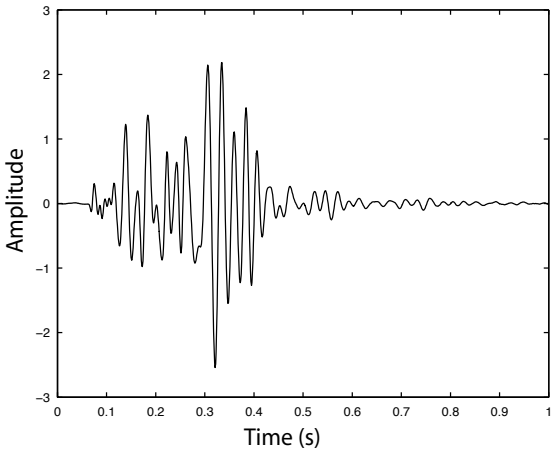

Figure 6. A single trace showing typical signal-to-noise ratio of first-break and surface-wave arrival (the latter at ≈0.28 seconds).

Surface-Wave Group Velocities

The 30-Hz instantaneous amplitude of the analytic signal for the same source-receiver pair as Figure 6 is shown in Figure 7. There are a number of local maxima besides the high-amplitude arrival at 0.3 seconds. Our automated picking scheme would locate all of these, up to a user-selected value, prioritizing by amplitude.

Figure 8 plots the analytic-trace amplitude for six frequencies for the same source-receiver pair. Note that the time axis has been converted to velocity. Within this one trace, some notable features are present. At 10 Hz, 30 Hz, and 60 Hz, only one pick is found, and it is interpreted to be the fundamental-mode Rayleigh-wave arrival. At 20 Hz, two picks are found. The smaller amplitude arrival interpreted as the first-higher Rayleigh-wave mode. At 40 Hz, multiple picks are found, but only one has an amplitude and velocity consistent with a surface-wave arrival. And at 50 Hz, again only one arrival is found, but with a velocity consistent with first-higher mode propagation. A broad shoulder in the 50-Hz trace gives a hint of the fundamental mode propagation.

The 50-Hz case in Figure 8 represents a challenge to an automated picking and inversion scheme. Simply assuming that the highest-amplitude arrival is the fundamental mode fails in this case and forwarding the traveltime to an inversion scheme would result in incorrect and unstable results. One way to eliminate spurious picks is to estimate, *a priori*, the fundamental-mode velocities for the region in question and only forwarding the proper picks to the tomographic algorithm. We accomplish this by simply plotting all picks at all frequencies for every source-receiver pair and ob-

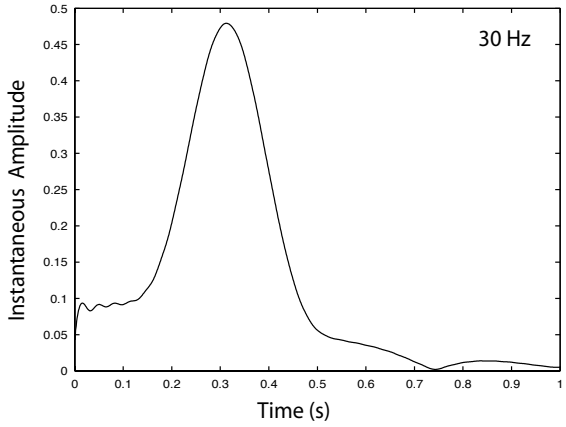

Figure 7. Instantaneous amplitude at 30 Hz of the trace in Figure 6.

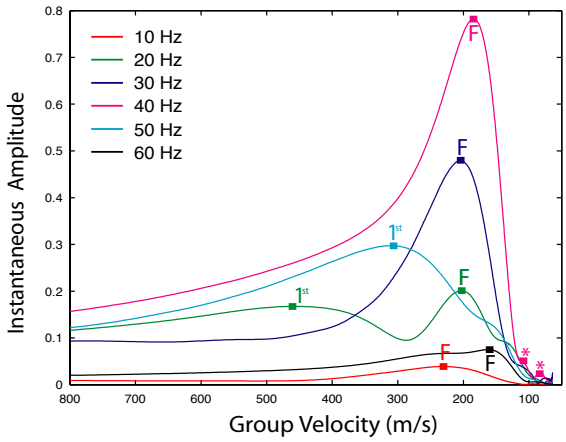

Figure 8. Instantaneous amplitudes of the trace in Figure 6 at six frequencies. The x-axis has been converted to velocity. "F's" indicate arrivals interpreted to be from the fundamental-mode Rayleigh wave. "1st's" represent arrivals interpreted to be from the first higher-mode Rayleigh wave. "$\star$'s" are other local maxima.

serving the trend of the arrivals (Figure 9). In Figure 9, warmer colors indicate more picks at that frequency-velocity coordinate. Two dispersive trends are evident. We interpret these as the fundamental and first-higher Rayleigh-wave modes. Using this plot, a time window was defined around the fundamental-mode Rayleigh-wave dispersion curve that captured 95% of the picks. Only those picks that fell within this time window were forwarded to the group-velocity tomography algorithm.

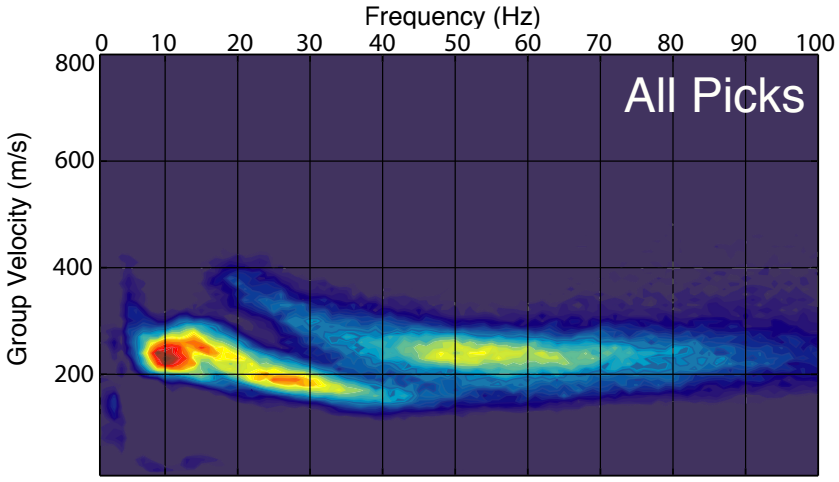

Figure 9. Plot of all local maxima picks. Warmer colors indicate more picks at that frequency-velocity coordinate. Two dispersive arrivals are evident, the curve with lower-velocities, is interpreted as representing the fundamental-mode Rayleigh wave.

Group-Velocity Tomography

Group-velocity tomograms were created with PRONTO at 1-Hz intervals from 10 Hz to 60 Hz (see Figure 10 for 4 of the 50 frequencies). All 50 planes create a 3-D velocity distribution when stitched vertically (Figure 11a).

Dispersion Curve Inversion

After the determination of the dispersion curve for each x, y coordinate (Figure 11b), it is inverted for shear-wave velocity with depth (Figure 11c). Then, analogous to the group-velocity tomography, the individual 1-D profiles are stitched together to form

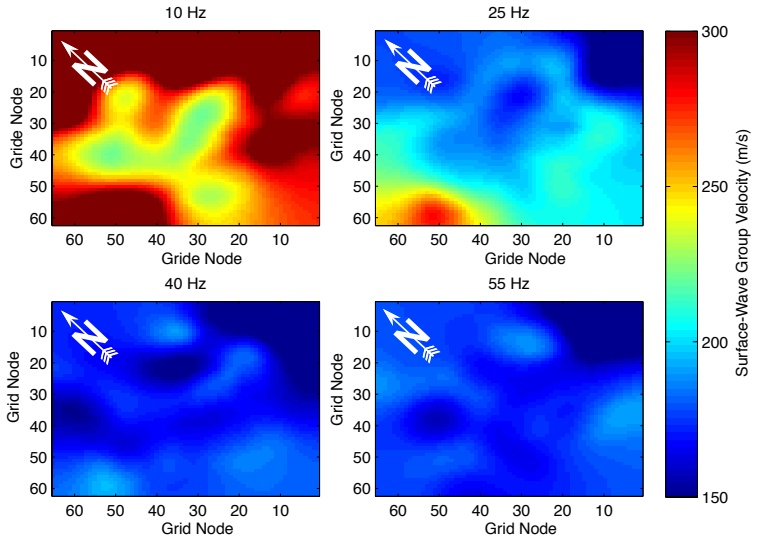

Figure 10. Group-velocity tomograms at four frequencies. Grid spacing is 1 meter.

a 3-D shear-wave velocity distribution (Figures 12, 13). The data was interpolated at a grid spacing of 2 meters in x, y, and z.

Refraction Velocity Optimization

The 3-D refraction velocity optimization is presented in Figures 14, and 15. Grid spacing is identical to the shear-wave velocity distribution (2 meters in x, y, z.)

Velocity Intepretation

The velocity tomograms (Figures 12-15) all show the expected increase in velocity with depth. The southeast corner of the FACT site shows higher velocities for both P- and S-waves. It is possible that this represents the footwall if one of the *en echelon*, down-to-the-east, normal faults that form the Hubbell Bench. Velocities are otherwise consistent with shallow alluvial deposits. The average shear-wave velocity in the upper 30 meters (the V_{30} parameter used in seismic hazard calculations (Frankel et al., 1996)) is 508 m/s. This places the FACT Site in the "C" Category (very stiff soil to soft rock), as defined by the National Earthquake Hazards Reduction Program (NEHRP) guidelines. This V_{30} value should be used with some caution, as the maximum depth-of-penetration for the surface-wave tomography was 31 meters. In most areas of the FACT Site, the depth-of-penetration was lower, in the upper 20s

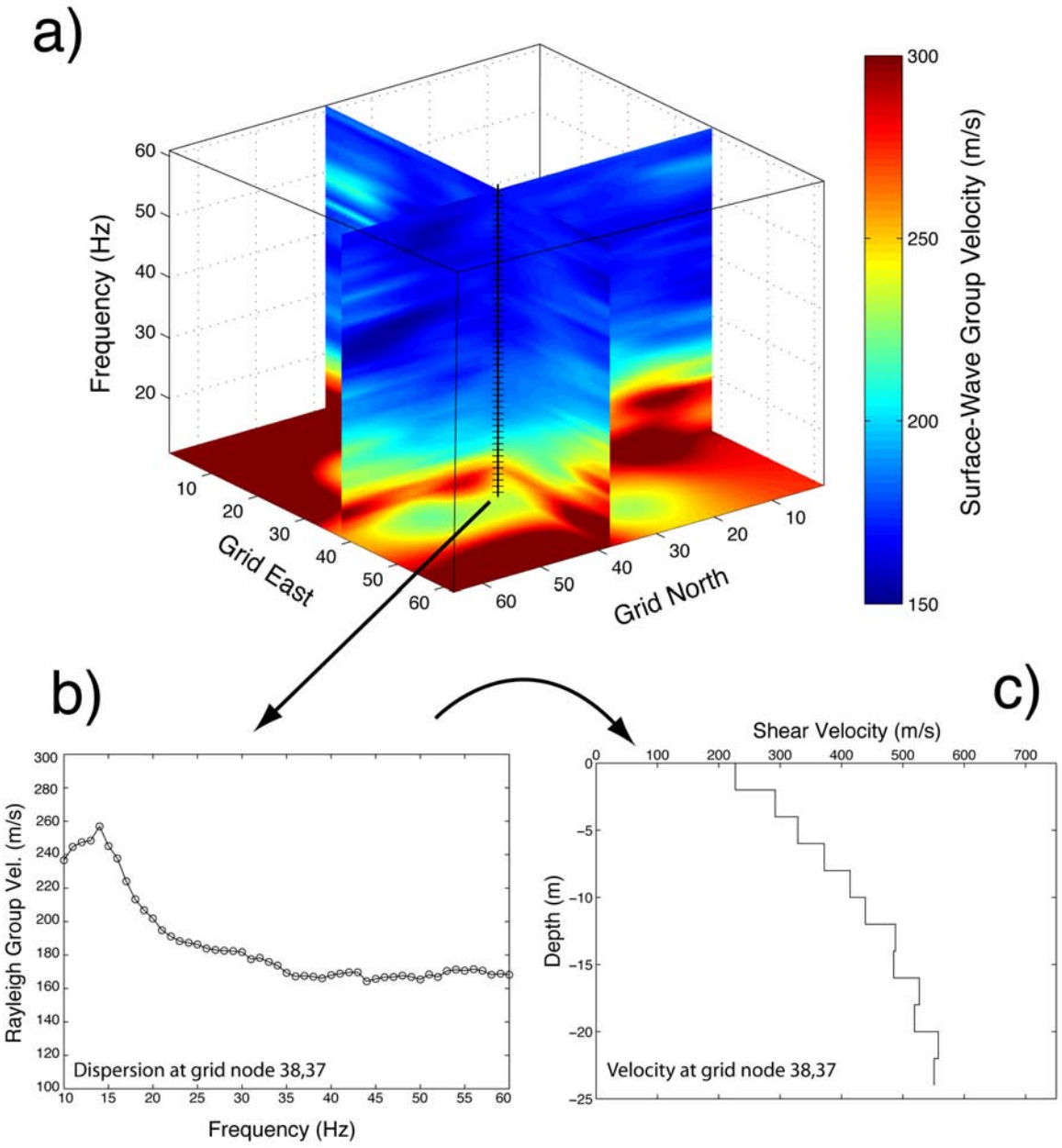

Figure 11. a) Three slices through the 3-D group-velocity tomogram. Black hatched line values are plotted in b). b) Fundamental-mode Rayleigh-wave dispersion curve. c) 1-D shear-wave velocity model after inversion of b), gridded to a uniform layer thickness of 2 meters.

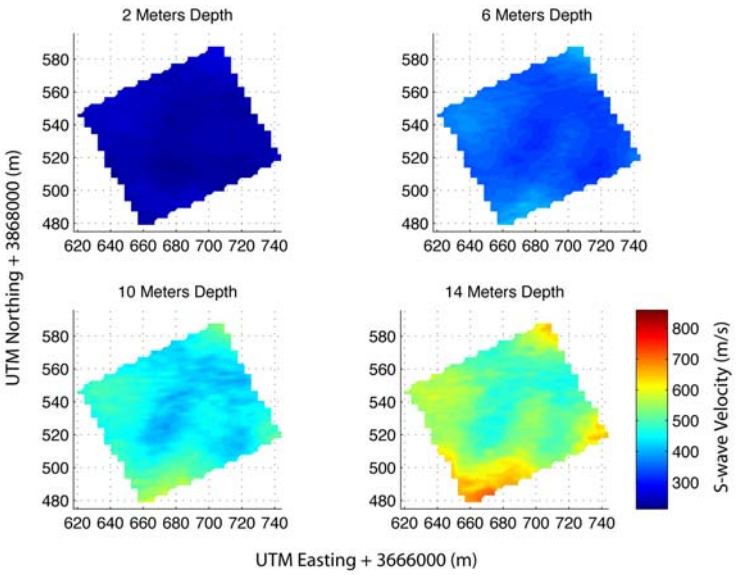

Figure 12. Shear-velocity tomograms at four depths.

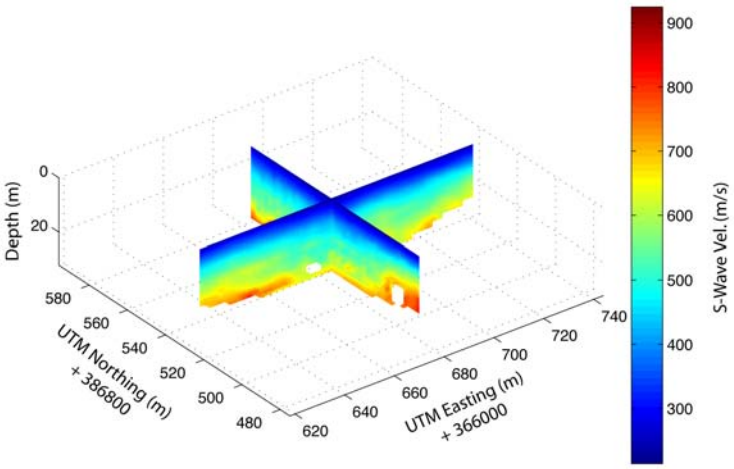

Figure 13. 3-D Shear-wave velocity.

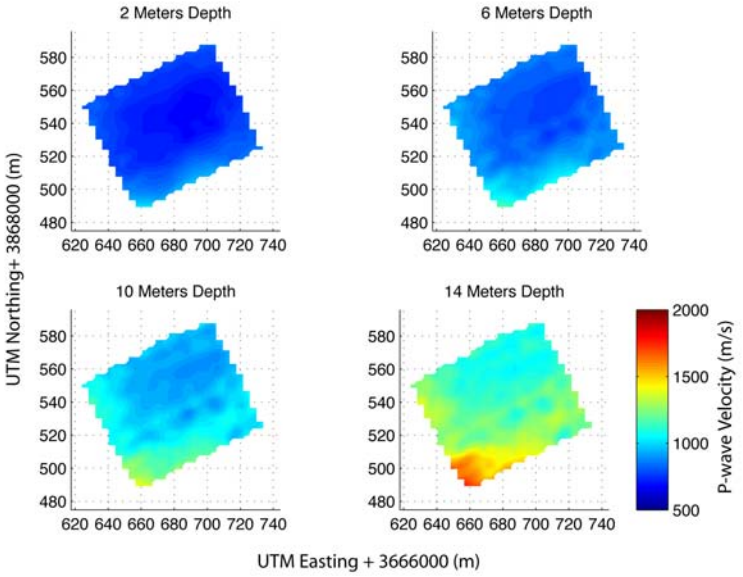

Figure 14. Compressive-velocity tomograms at four depths.

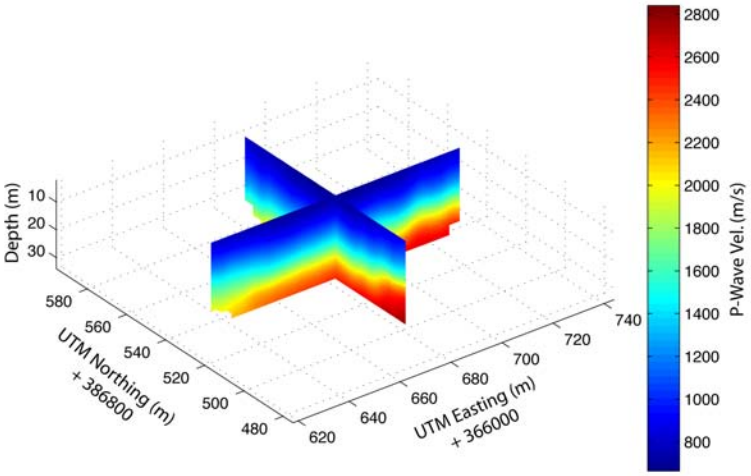

Figure 15. 3-D Compressive Velocity

of meters. If V_{30} is a parameter is viewed as an important parameter, then future studies should increase the aperture array beyond the 100 meters by 70 meters used here. P-wave tomography, on the other hand, penetrated deeper, with the deepest-diving waves traveling to 42 meters

V_p/V_s (Figures 16 and 17) decreases with depth, with values ranging from 3.2 to 2.2. A decrease in V_p/V_s is to be expected as soil porosity decreases with depth due to compaction. While both V_p and V_s should increase with compaction, V_s is more sensitive to porosity changes. For example, Domenico (1984) found that V_s in sandstone is 2 to 5 times more sensitive to porosity changes. The averaged value of 2.7 is consistent with the range of V_p/V_s found with suspension borehole logs under the ROSRINE Project (ResOlution of Site Response Issues from the Northridge Earthquake, `http://geoinfo.usc.edu/rosrine/Default.htm`). Average V_p/V_s in the upper 30 meters for 28 Los Angeles-area soil borings is 3.56 (standard deviation = 1.62).

Conclusions

We presented results from a seismic tomography experiment at the Facility for Analysis, Calibration, and Testing at Sandia National Laboratories, Albuquerque, New Mexico. Using the same array geometry and seismic source, we collected surface-wave and refraction data for a region measuring 70 meters by 100 meters. The data was inverted to obtain three-dimensional distributions of both shear-wave velocity and compressive-wave velocity. Maximum depth-of-penetration was approximately 30 meters. Average shear-wave velocity in the upper 30 meters (508 m/s) was found to be in the National Earthquake Hazards Reduction Program (NEHRP) "C" range (stiff soil). This agrees with the surface geology of the FACT Site (an older alluvial surface). Also in agreement with geologic mapping, we find indications of a down-to-the-east normal fault on the eastern edge of the site. The average ratio of compressive-velocity to shear-velocity V_p/V_s, was found to be 2.7, within the range of V_p/V_s found in other shallow soil studies.

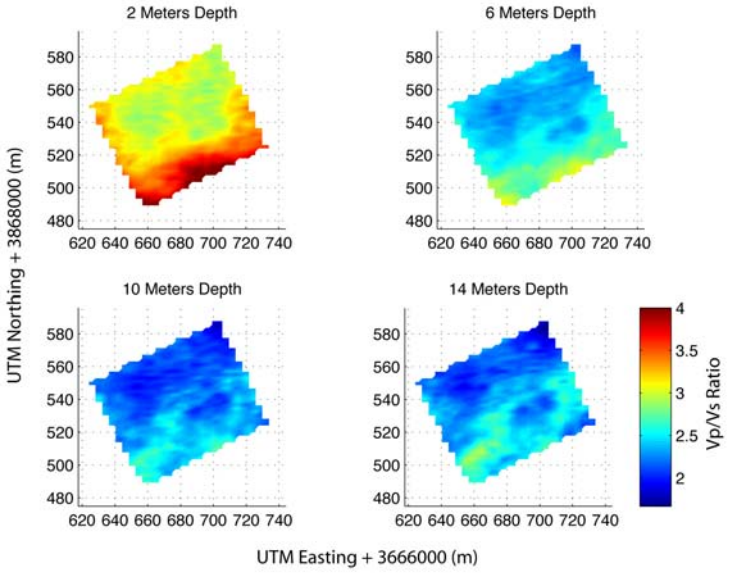

Figure 16. Vp/Vs at 4 depths.

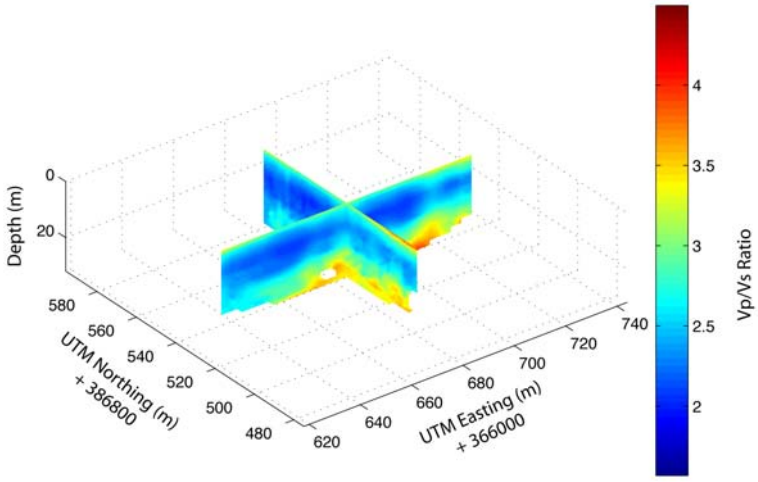

Figure 17. 3-D Vp/Vs Ratio

References

Aldridge, D. F., and Oldenburg, D. W., 1993, Two-dimensional tomographic inversion with finite-difference traveltimes: Journal of Seismic Exploration, **2**, no. 3, 257–274.

Arns, C. H., Knackstedt, M. A., and Pinczewski, W. V., 2002, Accurate Vp:Vs relationship for dry consolidated sandstones: Geophysical Research Letters, **29**, no. 8, 1202.

Chamberlin, R. M., Karlstrom, K. E., Connel, S. D., Brown, C., Nyman, M., Hitchcock, C., Kelson, K. I., Noller, J., Sawyer, T., Cavin, W. J., Parchman, M. A., Cook, C., and Sterling, J. Geology of the Mount Washington quadrangle, Bernallilo and Valencia Counties, New Mexico:, 2002.

Dane, C., and Bachman, G. O. Geologic map of New Mexico:, 1965.

Domenico, S. N., 1984, Rock lithology and porosity determination from shear and compressional wave velocity: Geophysics, **49**, 1188–1195.

Dziewonski, A., Bloch, S., and Landisman, M., 1969, A technique for the analysis of transient seismic signals: Bulletin of the Seismological Society of America, **59**, no. 1, 427–444.

Ensley, R. A., 1985, Comparison of P- and S-wave seismic data: a new method for detecting gas resevoirs: Geophysics, **49**, no. 9, 1420–1431.

Frankel, A. D., Mueller, C. S., Barnhard, T. P., Perkins, D. M., Leyendecker, E. V., Dickman, N., Hanson, S. L., and Hopper, M. G., National seismic-hazard maps; Documentation June 1996:, Open-File Report - U. S. Geological Survey OF 96-0532, U. S. Geological Survey, 1996.

Herrmann, R. B. Computer programs in seismology:, 2005.

Kocaoglu, A. H., and Long, L. T., 1993, A review of time-frequency analysis techniques for estimation of group velocities: Seismological Research Letters, **64**, no. 2, 157–167.

Louie, J. N., 2001, Faster, better: Shear-wave velocity to 100 meters depth from refraction microtremor arrays: Bulletin of the Seismological Society of America, **91**, no. 2, 347–364.

Maldonado, F., Connel, S. D., Love, D. W., Grauch, V. J. S., Slate, J. L., Mcinitosh, C., Jackson, P. B., and Byers Jr., F. M., 1999, Neogene geology of the Isleta Reservation and vicinity, Albuquerque Basin, central New Mexico *in* Pazzaglia,

F. J., and Lucas, S. G., Eds., Albuquerque Geology:: New Mexico Geologic Society, 175–188.

Nazarian, S., and Stokoe II, K. H., 1984, In situ shear wave velocities from spectral analysis of surface waves: San Francisco, CA, Proceedings of the World Conference on Earthquake Engineering, 21–28.

Olsen, K. H., Baldridge, W. S., and Callender, J. F., 1987, Rio Grande Rift: an overview: Tectonophysics, **143**, no. 1-3, 119–139.

O'Neill, A., and Matsuoka, T., 2005, Dominant higher surface-wave modes and possible inversion pitfalls: Journal of Environmental and Engineering Geophysics, **10**, no. 2, 185–201.

Park, C. B., Miller, R. D., and Xia, J., 1999, Multi-channel analysis of surface waves: Geophysics, **64**, no. 3, 800–808.

Pazzaglia, F. J., Woodward, L. A., Lucas, S. G., Anderson, O. J., Wegmann, K. W., and Estep, J. W., 1999, Phanerozoic geologic evolution of the Albuquerque area *in* Pazzaglia, F. J., and Lucas, S. G., Eds., Albuquerque Geology:: New Mexico Geologic Society, 97–114.

Personius, S. F., Machette, M. N., and Kelson, K. I., 1999, Quaternary faults in the Albuquerque area - an update *in* Pazzaglia, F. J., and Lucas, S. G., Eds., Albuquerque Geology:: New Mexico Geologic Society, 189–200.

Pullammanappallil, S. K., and Louie, J. N., 1994, A generalized simulated-annealing optimization for inversion of first-arrival times: Bulletin of the Seismological Society of America, **84**, no. 5, 1397–1409.

Tatham, R. H., 1982, Vp/Vs and lithology: Geophysics, **47**, no. 3, 336–344.

Vidale, J., 1988, Finite-difference calculation of travel times: Bulletin of the Seismological Society of America, **78**, no. 6, 2062–2076.

DISTRIBUTION:

5 Satish Pullammanappallil
Seismology Lab, University of Nevada, Reno, MS 174
1664 N. Virginia St., Reno, NV 89557-0141

1 Robert Reinke
Defense Threat Reduction Agency
1680 Texas Street SE
Kirtland AFB, NM 87117-5669

1 Robert Greschke
IRIS Passcal Instrument Center
New Mexico Tech
100 East Road
Socorro, New Mexico, 87801

5 MS 1168
Robert E. Abbott, 1647

1 MS 0750
David F. Aldridge, 6116

5 MS 0750
Lewis C. Bartel, 6116

1 MS 1168
Lalit Chhabildas, 1647

1 MS 0404
Eric P. Chael, 5736

1 MS 1168
Christopher Deeney, 1640

1 MS 0750
Greg J. Elbring, 6116

5 MS 0750
Bruce P. Engler, 6116

1 MS 1161
David R. Gardner, 5432

1 MS 0750
Matthew M. Haney, 6116

1 MS 0404
Richard P. Kromer, 05736

1 MS 1190
M. Keith Matzen, 1600

1 MS 1161
Terry K. Stalker, 5432

1 MS 0750
Neill P. Symons, 6116

2 MS 9018
Central Technical Files, 8944

2 MS 0899
Technical Library, 4536

1 MS 0123
D. Chavez, LDRD Office, 1011